nature immunology

Integration of the movement of signaling microclusters with cellular motility in immunological synapses

Peter Beemiller[1], Jordan Jacobelli[1,2] & Matthew F Krummel[1]

Immune synapses form between T cells and antigen-presenting cells (APCs). Increasing evidence suggests synapses must form flexibly to accommodate ongoing motility and displacement of the synapse. Here, time-lapse total internal reflection fluorescence (TIRF) microscopy showed that signaling via the T cell antigen receptor (TCR) occurred during synapse translation. TCR microclusters in motile synapses did not flow directly into supramolecular activating complexes (SMACs) but were directed, independently of myosin II contractility, toward an F-actin-poor 'sink' region. Inward microcluster flow often followed collapse of the leading edge, which suggested that actin depolymerization regulated microcluster flow and the formation of SMACs. The coordination of TCR movement with the translocation of this 'sink' shows how T cells coordinate TCR signaling and microcluster flow in dynamic physiological synapses.

T cells are activated when T cell antigen receptors (TCRs) bind to complexes of agonist peptide and major histocompatibility complex (pMHC) on antigen-presenting cells (APCs), which triggers the collection of TCRs into signaling microclusters with a size on the scale of micrometers[1,2]. Studies of synapse formation have shown that microclusters flow inward radially, coalescing into a large central supramolecular activating complex (cSMAC)[1,3,4]. Although cSMACs were initially suggested to be activating domains, it is now evident that signaling is supported mainly by peripheral microclusters[5–7]. The formation of microclusters and SMACs depends on the actin cytoskeleton[6,8]. Synapse formation also requires adhesive interactions between other surface receptors, such as LFA-1 (CD11a) on the T cell and ICAM-1 on the APC[9]. A surrounding adhesive domain of the synapse, called the 'peripheral SMAC', often shows enrichment for such interactions[2,4].

The initial antigenic stimulation is associated with ongoing T cell motility[10–12]. The resulting sequential interactions with APCs potentially allow T cells to 'sum' stimuli from encounters[11,13]. Such movements also suggest that immune synapses form against a continuously reorganizing cytoskeletal scaffold and that TCRs are sorted into flexible domains. Given the fluid nature of T cell–APC contacts observed *in vivo*, it is unclear how well the uniformly organized, stationary synapses often seen *in vitro* represent physiological immune synapses.

Although some progress has been made in the analysis of TCR reorganization in synapses *in situ*, technical constraints limit the spatiotemporal resolution possible there, which prevents the analyses needed to elucidate TCR dynamics relative to the cytoskeleton during motility. How actin dynamics organize microcluster flow during motility and how SMACs are positioned in motile synapses are not understood. Total internal reflection fluorescence (TIRF) microscopy of synapses formed on glass coverslip–supported lipid bilayers is ideally suited for the analysis of domain dynamics in motile synapses[2,14,15]. Much of this work, however, has been limited by the lack of model systems available for the analysis of motility during signaling *in vitro*.

Using a lipid bilayer system to activate OT-I T cells (which have transgenic expression of an ovalbumin-specific TCR), we investigated microcluster dynamics in synapses formed during motility. We analyzed a range of stationary and motile synapses, which allowed us to study the relationships among calcium signaling, microcluster dynamics, domain formation and motility. As observed *in vivo*[16,17], we found that the recognition of pMHC complexes resulted in lower T cell motility but did not strictly halt this movement. By analyzing the movement of microclusters, cSMACs and synapses, we found that that the flow of microclusters in motile synapses aligned with cell movement rather than moving toward existing cSMACs. The initiation of motility did not depend on cSMAC formation, but mature cSMACs moved in the direction of flowing TCRs and synapse motility. Through the use of genetically deficient mice and pharmacological inhibitors, we found that microcluster flow and the generation of a central actin 'sink' region did not require myosin II motors. Subsequent analysis of actin filament (F-actin) dynamics showed a correlation between F-actin clearance and inward microcluster movement. Actin depolymerization was needed to establish an F-actin-poor interior 'sink' region, toward which TCRs and cSMACs moved. Our results demonstrate that actin depolymerization and central clearance of F-actin organize the flow of TCRs from the periphery and provide a model for the formation of immune synapses applicable to both stable and transient T cell–APC interactions.

RESULTS

T cells coordinate TCR signaling with motility

Published studies have separately identified relationships between the avidity of the TCR-pMHC interaction and deceleration of cell motility,

[1]Department of Pathology, University of California, San Francisco, San Francisco, California, USA. [2]Present address: National Jewish Health, Denver, Colorado, USA. Correspondence should be addressed to M.F.K. (matthew.krummel@ucsf.edu).

Received 2 March; accepted 31 May; published online 1 July 2012; doi:10.1038/ni.2364

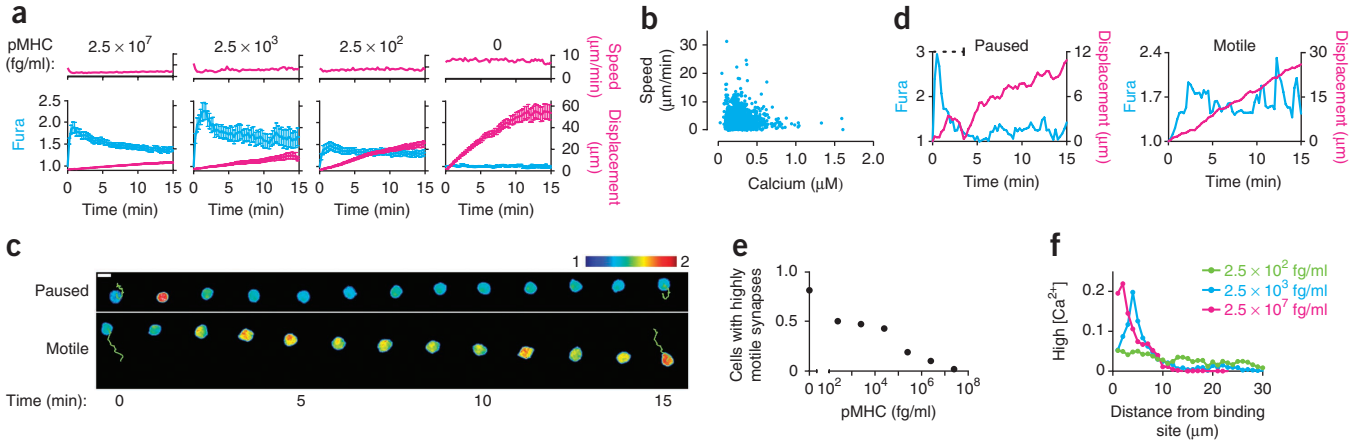

Figure 1 T cells remain motile during TCR signaling triggered by a large range of agonist doses. (**a**) Speed (above) and both calcium concentration (presented as normalized Fura-2 ratio) and displacement (below) of cells (>75 per condition) interacting with bilayers loaded with various concentrations of pMHC (top). (**b**) Speed and cytosolic calcium concentration of cells ($n = 96$) interacting with bilayers loaded with pMHC at a density of 2.5×10^3 fg/ml. (**c**) Image sequences of a paused synapse in which motility followed TCR signaling activity (top) and a motile synapse in which signaling occurred during motility (bottom); image intensities were scaled to a normalized Fura-2 ratio intensity range of 1–2, and images were filtered with a 0.4-μm σ Gaussian filter. Scale bar, 5 μm. (**d**) Fura-2 ratio and displacement of the cells in **c**. Dashed line (top left) indicates the calcium-correlated pause. (**e**) Fraction of cells that formed synapses of high motility (average speed, ≥3.8 μm/min) among the cells in **a** and from **Supplementary Figure 1** ($n = 776$ cells total). (**f**) Fraction of cells with a high calcium concentration ($[Ca^{2+}]$) (above the baseline Fura-2 ratio) among the cells in **a** versus cell displacement (binned into intervals of 1 μm relative to the site of bilayer binding). Data are from four experiments with two to four bilayers per condition (error bars (**a**), s.e.m.).

as well as TCR-mediated calcium influx and motility arrest[17,18]. However, with limited exceptions[17,19], studies of T cell activation on bilayers have analyzed arrested T cells and have not addressed the interaction of pMHC density, calcium signaling and motility. To determine whether supported bilayers can recapitulate some of the activation dynamics seen *in vivo*[10,11], we investigated the relationship among agonist density, TCR signaling and T cell motility on a bilayer system. We developed a bilayer system cushioned with polyethylene glycol, which we used to stimulate OT-I T cells that presented ICAM-1 and the SIINFEKL peptide of ovalbumin bound to H-2K^b MHC molecules (**Supplementary Fig. 1**). We generated bilayers with pMHC densities ranging from the density measured on reference APCs (bone marrow–derived dendritic cells (BMDCs) pulsed with agonist peptide) down to five orders of magnitude lower; we fixed ICAM-1 at a density similar to that on BMDCs (**Supplementary Fig. 1**).

Using the titrated bilayers described above, we analyzed how synapse motility and cytosolic calcium fluxes related to the density of TCR ligands. We measured cell displacement and intracellular calcium concentrations by time-lapse ratiometric imaging of the calcium indicator Fura-2 (ref. 20) for each pMHC density. On bilayers that presented pMHC complexes at densities similar to those of reference, peptide-pulsed BMDCs (that is, bilayers loaded with pMHC at a density of 2.5×10^7 fg/ml), OT-I T cell blasts generated immediate and robust calcium influx (**Fig. 1a**). The motility of those cells was much lower than that of cells on nonstimulating bilayers (**Fig. 1a**). However, cells moved at a relatively constant speed (1.9 μm/min). This effect was similar over three orders of magnitude of pMHC density (**Supplementary Fig. 1**). On bilayers loaded with 0.01% as much pMHC (2.5×10^3 fg/ml), cells still underwent a substantial increase in intracellular calcium, but overall cell speeds were twice as high (3.9 μm/min; **Fig. 1a**). At the lowest pMHC density studied (2.5×10^2 fg/ml), T cells still generated calcium fluxes, but calcium concentrations peaked at roughly half that observed at high doses of agonist. Cells crawling over such relatively low densities of agonist moved at about half the speed of cells on nonstimulating bilayers (3.8 μm/min versus 7.8 μm/min; **Fig. 1a**).

To quantify the relationship between cytosolic calcium and motility, we converted the ratiometric intensity of Fura-2 to the calcium concentration of the cells presented to bilayers loaded with pMHC at a density of 2.5×10^3 fg/ml. These cells were intermediately motile but generated maximal calcium fluxes (**Fig. 1a**). We then plotted the instantaneous cell speed versus calcium concentration for these cells (**Fig. 1b**). Consistent with published work[18], cell speeds were generally inversely proportional to calcium concentration, and calcium concentrations greater than ~0.75 μM resulted in arrest. However, cells with moderately higher calcium concentrations moved at relatively high speeds, which indicated that a higher intracellular calcium concentration associated with TCR recognition did not necessarily block motility. Together these results were in agreement with *in vivo* work demonstrating TCR-mediated 'deceleration' rather than 'arrest'[17].

Cell motility during engagement of the bilayer often had two types of prototypical patterns. In 'paused' interactions, calcium concentrations rapidly spiked during a period of limited cell movement (**Fig. 1c**,**d**). In contrast, during 'motile' interactions, calcium concentrations intermittently increased as the cell continuously moved without pauses (**Fig. 1c**,**d**). Individual cells had a range of motilities and calcium-flux activities and transition between modes. Such diversity led us to analyze how pMHC density affected the frequency of highly motile synapses and the amount of signaling generated during motility. As T cells on bilayers loaded with pMHC at a density of 2.5×10^3 fg/ml had much higher concentrations of intracellular calcium and relatively high motility, we characterized synapses that moved at greater than the median speed of those cells (≥3.8 μm/min) as being highly motile. We observed a dose-dependent decrease in the number of high-motility synapses ranging from 50% to 2% at the highest pMHC density (**Fig. 1e**). We then estimated the amount of calcium signaling generated relative to cell displacement. We normalized the time series of the ratiometric intensity of Fura-2 for all cells by the total, above-baseline ratiometric intensity signal detected. On bilayers with a high agonist density (2.5×10^7 fg/ml), ~45% of the total increased calcium signal that the cells generated occurred within 2 μm of

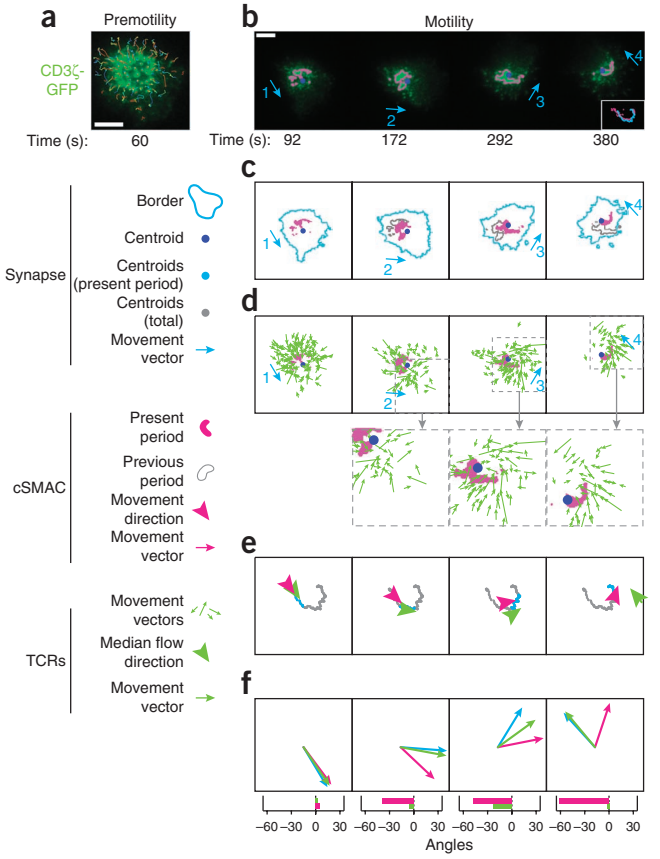

Figure 2 Microcluster flow aligns with movement in motile synapses. (**a**,**b**) Time-lapse TIRF images of a CD3ζ-GFP$^+$ OT-I T cell (of $n > 200$ total synapses) during synapse formation, showing microcluster paths before cell movement (**a**), and synapse motility divided into four periods based on the direction of movement (blue arrows); magenta indicates cSMAC borders (**b**). Inset (**b**), paths followed by the cSMAC and synapse centroids. Time (below) is relative to the start of TCR centralization. Scale bars, 5 μm. (**c**) The cSMAC (magenta), synapse border (light-blue) and cSMAC border at the end of the preceding motility period (gray) in the images in **b**. (**d**) Displacement vectors for microclusters formed during each motility period overlaid onto the cSMAC mask at the start of the period (magenta), for the images in **b**. Below, enlargement of areas outlined by dashed gray lines above. (**e**) Median microcluster flow direction (green) and direction of cSMAC movement (magenta) for each period in the images in **b**. Arrowhead points are positioned at the mean microcluster endpoint or cSMAC position at the end of the period. (**f**) Movement vectors for the cell (blue), cSMAC (magenta) and microclusters (green; median vector) in each period in the images in **b**, drawn with a common origin and scaled to the same magnitude (top); and angles between median microcluster movement vector and cell movement (green) and between cSMAC movement and cell movement (magenta) in each motility period (bottom). Data are representative of three experiments with six synapses that transitioned to motility.

binding sites (**Fig. 1f**). On bilayers loaded with pMHC at a density of 2.5×10^3 fg/ml, the peak in intracellular calcium shifted slightly, to ~4 μm from binding sites. At the lowest pMHC density (2.5×10^2 fg/ml), increases in intracellular calcium were not prominently localized to a particular distance from the binding site (**Fig. 1f**). Together these results indicated that although T cell speeds were generally modulated by the magnitude of TCR signaling, T cells interacting with the stimulating bilayers coordinated TCR signaling with motility.

TCR flow couples with cell motility

Having observed that T cells generated TCR signals in motile synapses, we determined whether the flow of TCR microclusters was also targeted to the cSMAC during motility, as predicted on the basis of stable synapses. To assess this, we tracked the movement of microclusters of the ζ-chain of the invariant signaling protein CD3 (CD3ζ) and green fluorescent protein (CD3ζ-GFP) by time-lapse TIRF microscopy of motile synapses formed by OT-I T cell blasts expressing CD3ζ-GFP[1,21]. We analyzed periods of motility after a premotile phase encompassing cSMAC formation (**Fig. 2a**,**b** and **Supplementary Movie 1**). We then compared the movement of TCR microclusters in arrested and motile synapses in individual cells.

Consistent with published studies of stationary synapses[2,6], TCRs generally flowed inward along radial courses before motility began, which resulted in a cSMAC (**Fig. 2a**). However, the symmetrical aspect of the synapse was quickly lost, which led to a motile synapse (**Fig. 2b** and **Supplementary Movie 1**). Using intensity-based masks to define the regions of the synapse (the footprint of the T cell on the bilayer) and cSMAC, we calculated the paths followed by each[22]. The direction of movement changed three times to create four motility periods (**Fig. 2b**). The cSMAC path generally tracked the movement of the cell, including changes in direction (**Fig. 2b**, inset), but it was not positioned centrally and lagged behind the synapse centroid (**Fig. 2c**).

We then analyzed microcluster movements to determine if they were directed toward the cSMAC during motility. This showed a pattern different from the premotility flow. Microcluster displacement vectors remained centripetally oriented. However, instead of flowing toward the cSMAC, microcluster vectors were shifted in the direction of motility and toward a region ahead of the cSMAC (**Fig. 2a**,**d**, insets). We noted this transition from cSMAC-oriented flow to motility-aligned flow for all motile synapses in which microcluster flow could be analyzed.

To quantify aggregate microcluster flow, we calculated the median displacement vector for all the microclusters formed in each motility period. We found that the direction of this vector typically aligned with the direction of synapse movement during that period (**Fig. 2e**). The movement vector for the cSMAC also tracked the movement vector for the synapse but often lagged relative to cell movement (**Fig. 2e**). Aggregate microcluster flow seemed to closely track synapse movement, even after changes in the direction of motility (**Fig. 2f**), whereas the movement vectors of the cSMAC and cells seemed loosely coupled and drifted apart over time (**Fig. 2f**, bottom). These data also suggested that microclusters and cSMACs moved toward a common, continuously moving target in motile synapses.

Central F-actin-poor region in motile synapses

We next analyzed whether synapse motility was dependent on cSMAC formation and whether cSMACs were generally motile structures. We examined the motile synapses formed by OT-I T cell blasts transduced with CD3ζ-GFP, analyzing the formation, positioning and movement of cSMACs relative to those of synapses. The cSMAC did not necessarily coalesce at the center of interfaces, even before motility, and cell displacement often seemed to begin before centralized TCR accumulations appeared (**Fig. 3a** and **Supplementary Movie 2**). In some synapses, cSMAC coalescence occurred as the cell transited the bilayer (**Fig. 3b**,**c**, motile cell), whereas in others, cSMACs aggregated before cell movement (**Fig. 3b**,**c**, paused cell). Alignment of image sequences by peak cSMAC areas and measurement of synapse speed versus normalized cSMAC area indicated no relationship between cSMAC

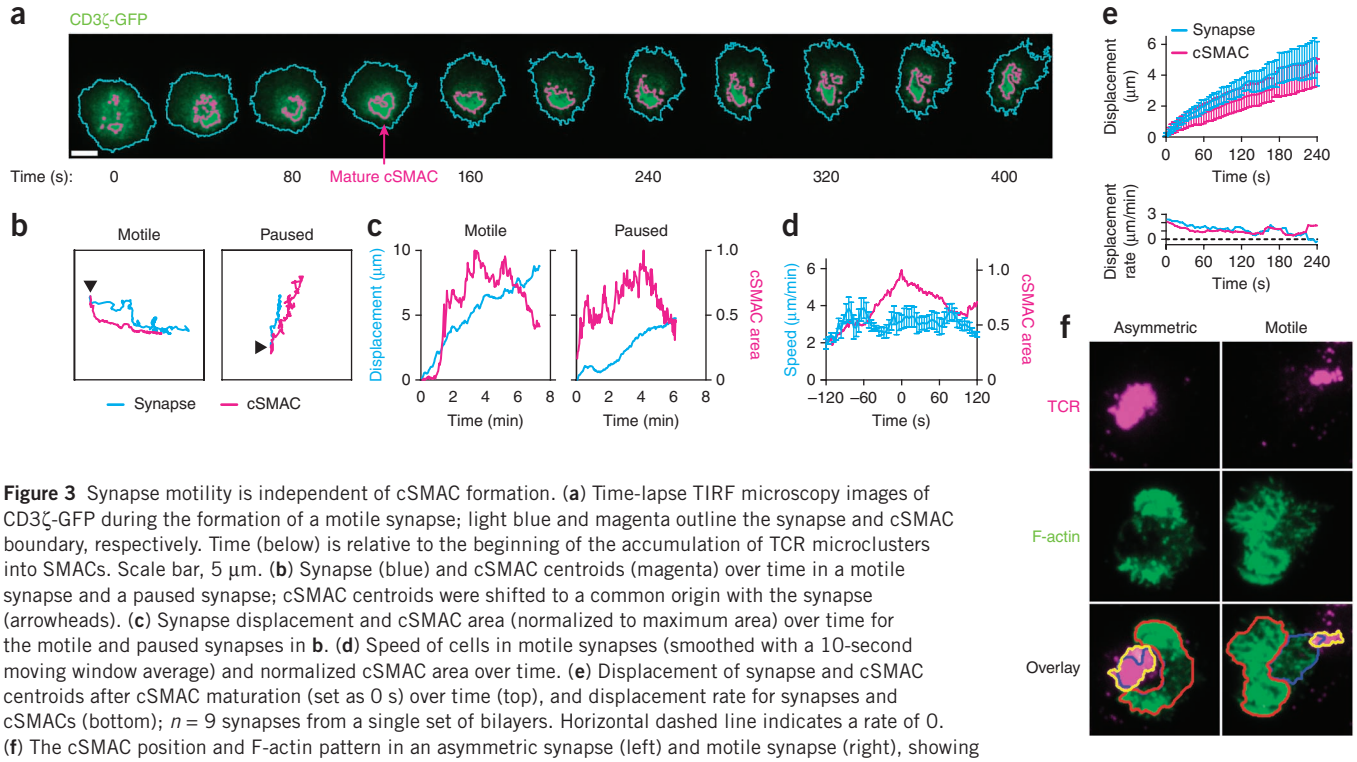

Figure 3 Synapse motility is independent of cSMAC formation. (**a**) Time-lapse TIRF microscopy images of CD3ζ-GFP during the formation of a motile synapse; light blue and magenta outline the synapse and cSMAC boundary, respectively. Time (below) is relative to the beginning of the accumulation of TCR microclusters into SMACs. Scale bar, 5 μm. (**b**) Synapse (blue) and cSMAC centroids (magenta) over time in a motile synapse and a paused synapse; cSMAC centroids were shifted to a common origin with the synapse (arrowheads). (**c**) Synapse displacement and cSMAC area (normalized to maximum area) over time for the motile and paused synapses in **b**. (**d**) Speed of cells in motile synapses (smoothed with a 10-second moving window average) and normalized cSMAC area over time. (**e**) Displacement of synapse and cSMAC centroids after cSMAC maturation (set as 0 s) over time (top), and displacement rate for synapses and cSMACs (bottom); $n = 9$ synapses from a single set of bilayers. Horizontal dashed line indicates a rate of 0. (**f**) The cSMAC position and F-actin pattern in an asymmetric synapse (left) and motile synapse (right), showing the border of the region of high F-actin density (red), the border of the F-actin-poor region (blue) and the cSMAC (yellow); $n = 29$ synapses (characterized as symmetric (data not shown), asymmetric (~30%) or motile (~40%)). Data are representative of three experiments (average and s.d. in **d**,**e**).

aggregation and the onset of motility (**Fig. 3d**). The displacement of mature cSMACs was slightly lower than the displacement of the cell, which resulted in positioning of the cSMAC at the trailing edges of motile synapses (**Fig. 3e**).

To visualize cSMAC positioning relative to F-actin distribution in asymmetric and motile synapses, we fixed T cells after synapse formation, then made the cells permeable and stained them with an Alexa Fluor 568–conjugated H57-597 antibody to TCRβ (anti-TCRβ) and Alexa Fluor 488–phalloidin. In asymmetric synapses, cSMACs occupied an F-actin-poor region near, but offset from, the center of synapses (**Fig. 3f**). In more polarized synapses characteristic of motility, cSMACs were positioned at the trailing edge of a cleared actin region (**Fig. 3f**), which occupied the interior of synapses. These results indicated that in mature cSMACs, the F-actin-poor interior was centrally located in motile synapses and that cSMACs trailed those domains.

Myosin II is dispensable for TCR centralization and synapse motility

Having established that TCR microclusters and cSMACs moved toward an F-actin-poor 'sink' region, we sought to identify cytoskeletal factors that oriented these movements and formed this domain. Although successful cSMAC development after inhibition of myosin II has been reported[23], myosin II has been reported to be essential for the signaling and movement of microclusters into cSMACs[24] or moderately important for the TCR centralization rate[25,26]. To determine whether myosin II regulated TCR centralization or general actin architecture in motile synapses, we treated OT-I T cell blasts for 30 min with the vehicle DMSO (control) or the negative enantiomer of blebbistatin, an inhibitor of myosin II (ref. 27), at a concentration of 50 μM, then introduced the cells to stimulating bilayers. After synapse formation, we fixed the cells and stained them to image the distribution of TCRs and F-actin. In mature control synapses, F-actin was abundant in the periphery and TCRs accumulated in the F-actin-poor interior (**Fig. 4a**). In asymmetric synapses, suggestive of polarization and motility, the F-actin-poor region and cSMAC were positioned at the posterior. In cells treated with blebbistatin, the generation of the F-actin-poor region and cSMACs was not affected (**Fig. 4a**). Likewise, in asymmetric synapses, repositioning of the F-actin-poor region and cSMAC to the posterior was not blocked.

Next we assessed the effect of blebbistatin on synapse motility. We loaded cells with the dye CellTracker Orange and imaged them on stimulating bilayers with illumination at a wavelength range of 555 ± 14 nm to avoid blebbistatin-mediated crosslinking with light at a wavelength of ~491 nm (refs. 28,29; **Supplementary Movie 3**). Blebbistatin diminished the median synapse speed from 2.0 μm/s to 1.6 μm/s (**Fig. 4b**), consistent with a role for myosin II in regulating crawling speed[30]. However, blebbistatin did not delay the onset of motility (**Fig. 4c**), which indicated that myosin II was not required for the initiation of synapse motility.

We then addressed whether myosin II regulated microcluster movements. To complement the drug approach, we used a system of conditional deletion of myosin II in OT-I T cell blasts derived from mice with *lox*P-flanked alleles encoding myosin IIA ($Myh9^{fl/fl}$)[31]. In this system, retroviral transduction of $Myh9^{fl/fl}$ cells with a construct encoding Cre recombinase linked to GFP (Cre-GFP) results in excision of the gene encoding myosin IIA, the only myosin II expressed in T cells[23]. Analysis of $Myh9^{fl/fl}$ cells that were transduced with Cre-GFP (cKO cells) indicated that these cells were typically depleted of myosin II to an abundance 20–30% that in control $Myh9^{fl/fl}$ OT-I T cells transfected to express GFP alone and subjected to the same transduction and sorting procedure (**Supplementary Fig. 2**). To image the dynamics of TCR microclusters in these cells, we stained TCRs with nonblocking Alexa Fluor 568–H57-597 before introducing them onto the bilayers (**Supplementary Fig. 2**).

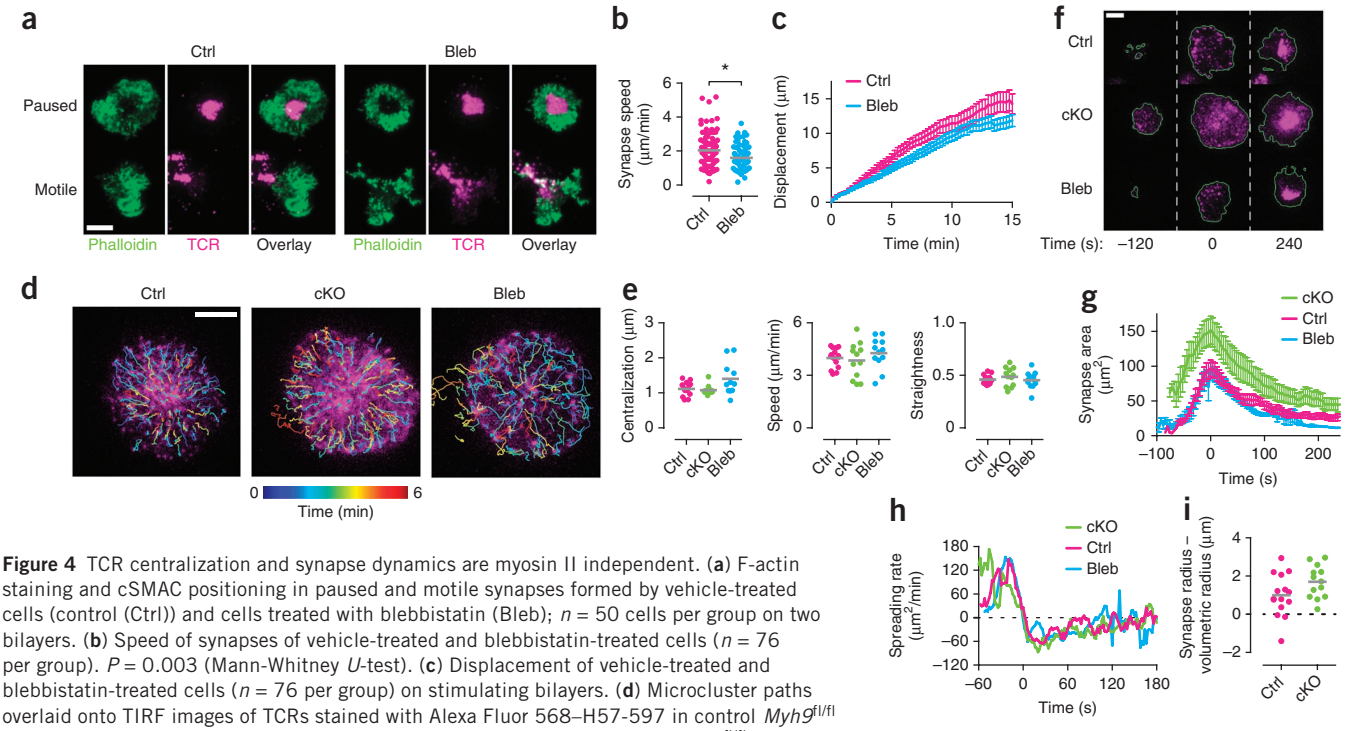

Figure 4 TCR centralization and synapse dynamics are myosin II independent. (**a**) F-actin staining and cSMAC positioning in paused and motile synapses formed by vehicle-treated cells (control (Ctrl)) and cells treated with blebbistatin (Bleb); $n = 50$ cells per group on two bilayers. (**b**) Speed of synapses of vehicle-treated and blebbistatin-treated cells ($n = 76$ per group). $P = 0.003$ (Mann-Whitney U-test). (**c**) Displacement of vehicle-treated and blebbistatin-treated cells ($n = 76$ per group) on stimulating bilayers. (**d**) Microcluster paths overlaid onto TIRF images of TCRs stained with Alexa Fluor 568–H57-597 in control *Myh9*$^{fl/fl}$ OT-I T cells transfected to express GFP alone (left), cKO cells (middle) and *Myh9*$^{fl/fl}$ OT-I T cells transfected to express GFP alone and then treated with blebbistatin (right). (**e**) Centralization (left), microcluster track speed (middle) and track straightness (right) of microclusters in control cells ($n = 16$), cKO cells ($n = 12$) and blebbistatin-treated cells ($n = 12$) as in **d**. $P < 0.05$, track parameters (one-way analysis of variance). (**f**) Spreading dynamics of control, cKO and blebbistatin-treated cells as in **d**. Time (below) is relative to the time at which maximum synapse area was achieved. (**g**) Synapse areas of control, cKO and blebbistatin-treated cells ($n = 7$ per group; as in **d**) over time. (**h**) Temporal derivative of the synapse areas; rates were smoothed with a 10-second moving average filter. Time (**g**,**h**), as in **f**. (**i**) Synapse radius minus volumetric radius for *Myh9*$^{fl/fl}$ cells transfected to express GFP alone (Ctrl; $n = 15$) and cKO cells ($n = 14$). $P = 0.116$ (Mann-Whitney U-test). Scale bars (**a**,**d**,**f**), 5 μm. Each symbol (**b**,**e**,**i**) represents an individual cell; small horizontal lines indicate the median (**b**,**e** (left), **i**) or mean (**e**, middle and right). Data are representative of one experiment (**a**–**c**,**i**) or three experiments (**d**–**h**); error bars (**c**,**g**), s.e.m.).

Tracking of TCR microclusters in control *Myh9*$^{fl/fl}$ cells transfected to express GFP alone, cKO cells and blebbistatin-treated *Myh9*$^{fl/fl}$ cells transfected to express GFP alone indicated that centralization of TCRs was not affected by genetic or chemical interference with myosin II (**Fig. 4d** and **Supplementary Movie 4**). To quantify inward flow, we calculated centralization values for the microclusters[22]. Median microcluster centralization, speed and track straightness were not substantially affected by treatment with blebbistatin or conditional deletion of myosin II (**Fig. 4e**).

To test for a defect in 'tensioning' (the application of a force to create stretch)[25], we compared the spreading of the control, cKO and blebbistatin-treated cells described above on stimulating bilayers. In all three conditions, cells rapidly spread microcluster-rich synapses. Over time, synapse areas contracted and cSMACs formed. Neither treatment with blebbistatin nor genetic ablation of myosin II blocked this spreading dynamic or cSMAC coalescence (**Fig. 4f**). The cKO cells generated greater synapse areas than the control cells did, but the blebbistatin-treated cells did not. However, synapse expansion and contraction seemed to proceed normally in cKO cells (**Fig. 4g**). Notably, the rate of expansion was not affected by either method of inhibiting myosin II (**Fig. 4h**).

To determine whether the greater synapse areas of the cKO cells might represent a specific defect in myosin II–mediated tensioning, we measured synapse sizes of control *Myh9*$^{fl/fl}$ cells transfected to express GFP alone and cKO cells relative to cell volume[22]. We found that cKO cells had a small, statistically insignificant greater mean synapse radius relative to the volumetric radius than control cells had (**Fig. 4i**), consistent with results demonstrating that myosin II does not modulate synapse area during TCR signaling[30]. As control and blebbistatin-treated cells generated identical synapse areas (**Fig. 4g**), we attribute the larger synapse area of the cKO cells to the greater size of cells depleted of myosin II (**Supplementary Fig. 2**).

Clearance of F-actin from synapse centers

The accumulation of TCRs in F-actin-poor regions independently of myosin II activity led us to analyze F-actin dynamics in spreading synapses. To image actin dynamics in living cells, we used Lifeact-GFP, a small protein probe that binds to F-actin nondisruptively and 'reports' the subcellular density of F-actin[32]. The rate of change in the intensity of Lifeact-GFP indicates whether a region is undergoing net actin polymerization or actin depolymerization.

To image F-actin dynamics during synapse spreading, we retrovirally transduced OT-I T cell blasts with Lifeact-GFP and stained the cells with Alexa Fluor 568–H57-597, then introduced the cells onto stimulating bilayers. During spreading, we observed a band of greater Lifeact-GFP intensity at the periphery (**Fig. 5a**), indicative of a region of high F-actin density. We then analyzed F-actin dynamics in the interior relative to that in a 2-μm 'edge' region located beyond that band (**Fig. 5a**,**b**). This edge region corresponded to the distal SMAC or lamellopodial region[26]. We plotted the intensity of Lifeact-GFP and edge-region position along a line through one side of the expanding synapse (**Fig. 5c**). As the edge expanded outward, the Lifeact-GFP region of high intensity moved outward, consistent with actin polymerization–driven expansion

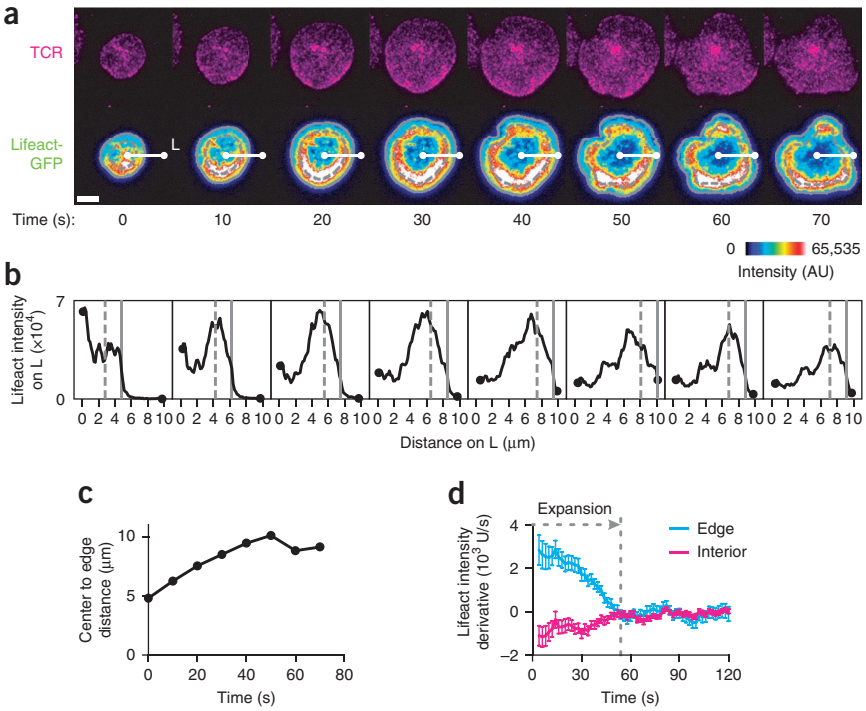

Figure 5 The polymerization and depolymerization of actin organizes synapses. (**a**) Time-lapse TIRF microscopy of a Lifeact-GFP$^+$ OT-I T cell blast spreading onto a stimulating bilayer (bottom), and Alexa Fluor 568–H57-597 labeled TCRs in the cell (top). Numbers below image are time (s). Scale bar, 5 μm. Intensity (key) is presented in arbitrary units (AU). (**b**) Linescan intensity for the 10-μm line 'L' in **a** (average of 3 pixels (0.48 μm)). Solid gray lines, synapse border; dashed gray lines, edge-interior border (2 μm from cell edge). (**c**) Distance to cell edge along the line 'L' in **a**. (**d**) Change in Lifeact-GFP intensity over time in the 1-μm^2 regions around the interior and edge microclusters in **a**; dashed vertical line indicates end of spreading period. Data are representative two experiments with eight synapses total (error bars (**d**), s.e.m.).

of the edge (**Fig. 5c**,**d**). Behind the spreading F-actin-dense band, F-actin abundance decreased during the first 30 s (**Fig. 5a**,**c**), which suggested depolymerization.

We then quantified changes in actin density in regions 1 μm^2 in area surrounding microclusters, separating the microclusters into two groups on the basis of whether the microcluster formed in the edge or interior region. In the edge region, the intensity of Lifeact-GFP increased until the end of spreading (**Fig. 5d**), which indicated that actin polymerization occurred throughout spreading. In the interior, the derivative of the Lifeact-GFP intensity was negative during expansion (**Fig. 5d**), which indicated active clearance of F-actin from the interior. This finding indicated that coordinated polymerization and depolymerization of actin organized synapse domains and suggested that regional depolymerization might establish a low-density 'sink' that directs TCR flow.

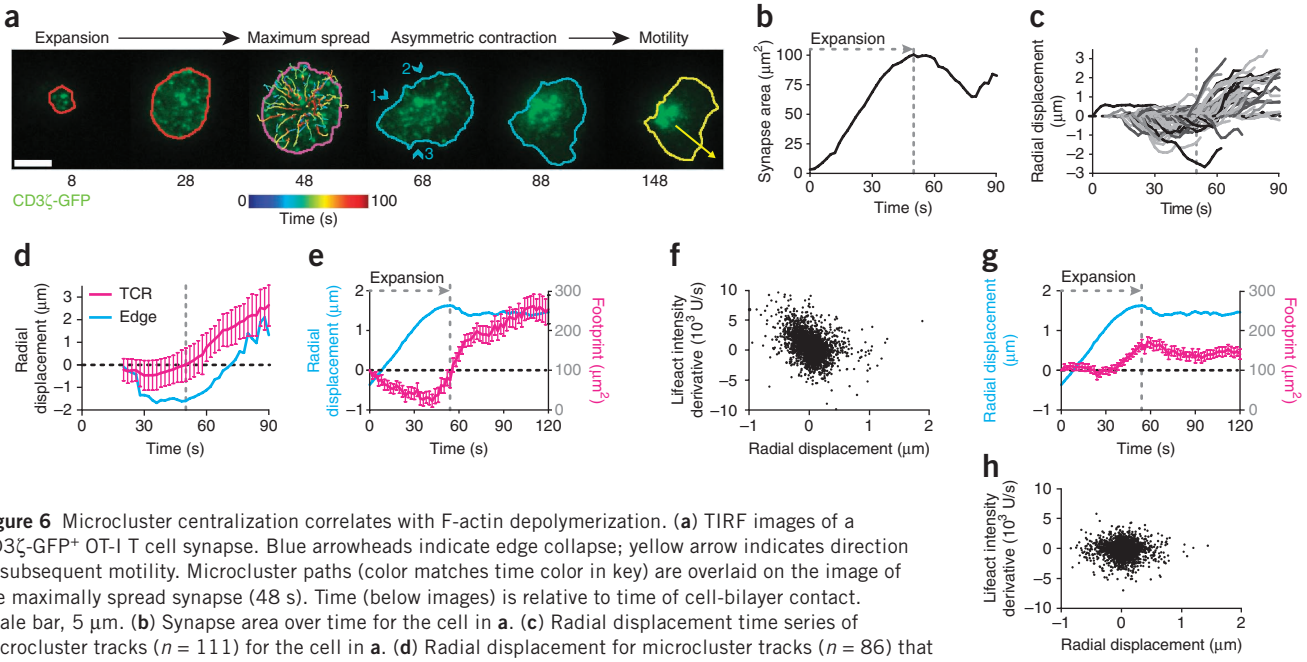

Figure 6 Microcluster centralization correlates with F-actin depolymerization. (**a**) TIRF images of a CD3ζ-GFP$^+$ OT-I T cell synapse. Blue arrowheads indicate edge collapse; yellow arrow indicates direction of subsequent motility. Microcluster paths (color matches time color in key) are overlaid on the image of the maximally spread synapse (48 s). Time (below images) is relative to time of cell-bilayer contact. Scale bar, 5 μm. (**b**) Synapse area over time for the cell in **a**. (**c**) Radial displacement time series of microcluster tracks (n = 111) for the cell in **a**. (**d**) Radial displacement for microcluster tracks (n = 86) that spanned the expansion-contraction process (TCR) and for the synapse edge (Edge) at points associated with microclusters, for the cell in **a**. (**e**) Radial displacement of microclusters that formed within 2 μm of the synapse edge during synapse spreading by a Lifeact-GFP$^+$ T cell. (**f**) Correlation between Lifeact-GFP intensity changes in 1-μm^2 regions centered on edge microclusters and microcluster radial movements. Movement toward the synapse center is positive; outward movement is negative. (**g**) Radial displacement of microclusters that formed in the interior during synapse spreading by a Lifeact-GFP$^+$ T cell. (**h**) Correlation between Lifeact-GFP intensity changes in 1-μm^2 regions centered on interior microclusters and microcluster radial movements (movements as in **f**). Dashed vertical lines (**b**–**e**,**g**) indicate time of maximum synapse area. Data are representative of three experiments with 11 synapses total (**a**–**d**; average and s.d. in **d**) or two experiments with eight synapses total (**e**–**h**; average and s.e.m. in **e**,**g**).

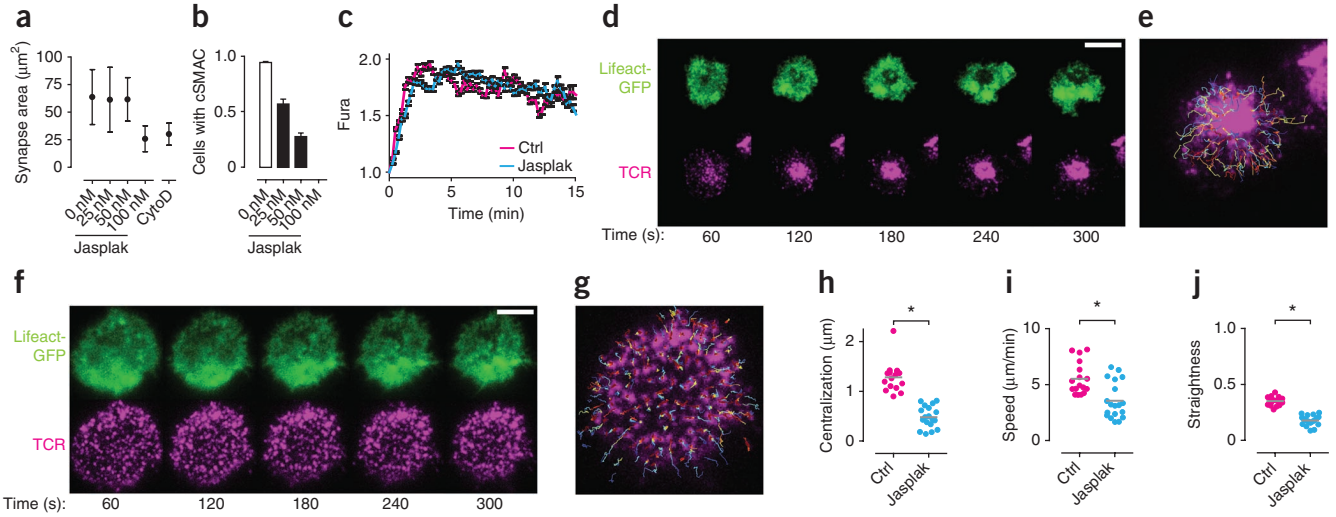

Figure 7 TCR centralization requires actin depolymerization. (**a**) Synapse areas formed by OT-I T cell blasts (n = 90–120 total) after treatment with DMSO vehicle (0 nM), various concentrations (horizontal axis) of jasplakinolide (Jasplak), or 10 μM cytochalasin D (CytoD). (**b**) OT-I T cell blasts (among n = 90–120 total) that formed cSMACs after treatment with DMSO or jasplakinolide. (**c**) Calcium fluxes generated by Fura-2-loaded OT-I T cell blasts (n = 30 per group) on stimulating bilayers after treatment with DMSO (Ctrl) or 50 nM jasplakinolide (Jasplak). (**d**) TIRF images of Lifeact-GFP (top) and TCRs (bottom) during synapse formation by a control OT-I T cell blast treated with DMSO; time (below) is relative to the start of spreading. Scale bar, 5 μm. (**e**) Microcluster paths overlaid onto images in **d**. (**f**) TIRF images of Lifeact-GFP (top) and TCRs (bottom) during synapse formation by an OT-I T cell blast treated with 50 nM jasplakinolide; time (below) as in **d**. Scale bar, 5 μm. (**g**) Microcluster paths overlaid onto images in **f**. (**h**–**j**) Microcluster centralization (**h**), microcluster track speed (**i**) and track straightness (**j**) during synapse formation by control cells treated with DMSO (n = 16) and cells treated with 50 nM jasplakinolide (n = 18). Each symbol (**h**–**j**) represents an individual cell; small gray horizontal lines indicate the mean. $P < 0.009$, in **h**–**j** (Student's t-test). Data are representative of two experiments with four bilayers (**a**,**b**; error bars, s.d. (**a**) or s.e.m. (**b**)), one experiment with four bilayers (**c**; error bars, s.e.m.), or three experiments with two bilayers (**d**–**j**).

Correlation of TCR centralization with depolymerization

We next analyzed the movement of TCR microclusters relative to synapse spreading and formation of the F-actin-poor 'sink' region. We first examined microcluster movement relative to synapse dynamics in CD3ζ-GFP$^+$ OT-I T cell blasts. Microcluster formation began immediately, and, as spreading completed, localized retractions began reshaping the synapse into a polarized structure (**Fig. 6a**,**b**). In many cells, we observed that edge collapse correlated with localized loss of F-actin and inward microcluster movement (**Supplementary Fig. 3**).

During spreading, TCRs, particularly those located near synapse edges, tended to move outward with the edges (**Supplementary Movie 5**). To quantify the kinetics of microcluster centralization, we calculated the radial movements of the microclusters relative to the synapse center[22] (**Supplementary Fig. 3**). We defined radial displacement value so that movements toward the cSMAC were positive and movements away from the cSMAC were negative. To analyze the relationship between movements of the edge and movements of the microcluster, we calculated edge displacement at the cell edge proximal to each of the 111 microcluster tracks (the distance to the edge along the line from the cSMAC centroid and through the microcluster). Radial displacements were directed outward during spreading and transitioned to inward movement as the synapse approached its peak area (**Fig. 6b**,**c**). As expansion ended, microcluster and edge radial displacements began increasing (**Fig. 6c**,**d**). This result indicated that TCR microcluster flows were sensitive to the same conditions that regulated the expansion and contraction of synapses.

Next we compared microcluster movements in the edge and interior relative to the instantaneous changes in F-actin density in the 1-μm^2 regions around microclusters with Lifeact-GFP[22]. Edge microclusters initially moved inward rapidly (3.9 μm/min) and then more slowly (1.1 μm/min) as they reached the interior of the synapse (**Fig. 6e**). When we analyzed the changes in F-actin density around edge microclusters relative to microcluster movements, we observed the following correlation: whereas outward displacement of microclusters, which occurred mainly during spreading, accompanied increasing F-actin density, inward movement was associated with movement into regions with relatively lower F-actin density (**Fig. 6f**, $r = -0.36$, and **Supplementary Fig. 3** and **Supplementary Movie 6**). This suggested that local polymerization in the distal SMAC did not drive the inward flow of local microclusters.

Interior microclusters underwent little radial displacement during spreading and did not begin to centralize for about 30 s (**Fig. 6g**). In contrast to the movement of edge microclusters, interior microcluster flow did not correlate with changes in actin density (**Fig. 6h**, $r = -0.02$). However, the centralization of interior microclusters began around the time that the F-actin-poor 'sink' region appeared, which suggested it was important for centralization.

TCR centralization requires actin depolymerization

To determine whether the formation of the regions of low F-actin density regulated the flow of TCR microclusters, we specifically blocked actin depolymerization in T cells interacting with stimulating bilayers. Although many inhibitors of actin polymerization are available, jasplakinolide specifically blocks depolymerization in living cells by binding to and stabilizing actin filaments[33]. However, the effects of jasplakinolide are complex; at low doses, filaments are stabilized, which inhibits depolymerization, whereas at high doses, jasplakinolide considerably alters cytoskeletal architecture and blocks polymerization[34]. Therefore, we developed a jasplakinolide treatment that did not inhibit synapse spreading, which is an actin polymerization–dependent process[35]. We stained OT-I T cell blasts with Alexa Fluor 568–H57-597 and the membrane dye DiO and treated the cells for 15 min on ice with various concentrations of jasplakinolide, then added the cells to bilayers. After treatment with jasplakinolide at

concentrations of up to 50 nM, cells showed no defect in spreading relative to that of control cells treated only with DMSO (**Fig. 7a**). After treatment with jasplakinolide at a concentration of 100 nM, however, synapse areas were 40% smaller than those of control cells, equivalent to synapses formed after direct inhibition of polymerization with cytochalasin D (**Fig. 7a**), which was indicative of impaired actin polymerization.

Jasplakinolide also inhibited cSMAC coalescence in a dose-dependent manner (**Fig. 7b**). At a concentration of 100 nM, jasplakinolide rendered T cells completely unable to generate cSMACs. Cells treated with jasplakinolide at a concentration of 50 nM, which did not block polymerization, had a much lower efficiency of cSMAC formation that was 30% the efficiency of control cells (**Fig. 7b**). Inhibition of depolymerization and cSMAC formation did not block TCR signaling, however, as control cells and cells treated with jasplakinolide at a concentration of 50 nM generated nearly identical calcium fluxes (**Fig. 7c**). We then did time-lapse TIRF microscopy of Lifeact-GFP and TCRs in OT-I T cell blasts treated with vehicle (control) or 50 nM jasplakinolide. In control cells, F-actin-poor interior regions appeared as TCR microclusters began to centralize (**Fig. 7d**,**e**). In motile synapses, cSMACs were positioned behind this F-actin-poor region (**Supplementary Movie 7**). Jasplakinolide-treated cells also spread actin-rich footprints onto bilayers and generated TCR microclusters (**Fig. 7f**). However, the F-actin-poor 'sink' region failed to form in the jasplakinolide-treated cells, and there was much less centralization of TCR microclusters than in control cells (**Fig. 7f**,**g**). Microcluster centralization (**Fig. 7h**) and speed (**Fig. 7i**) were significantly lower after treatment with 50 nM jasplakinolide than in control cells. In addition, the straightness of microcluster tracks was significantly lower in jasplakinolide-treated cells than in control cells (**Fig. 7j**), which suggested that microclusters that formed in the presence of jasplakinolide experienced greater confinement. These results demonstrated that actin depolymerization directed microcluster flow into regions of low F-actin density.

DISCUSSION

The coordinated flow of microclusters into a single central accumulation of TCRs would seem to indicate that the cSMAC serves as the organizational center of immune synapses. However, this model has not been used before, to our knowledge, to describe how T cells organize TCR clusters during dynamic interactions[11,13]. Here we were able to examine the dynamics of TCR microclusters in a motile setting, capturing an aspect of *in vivo* T cell activation that has been missing from *in vitro* studies. Although bilayers present an unlimited, uniform activation surface, *in vivo*, T cells may establish and break contacts with multiple, irregularly shaped DCs. Therefore, the importance of continued motility and myosin motor–mediated generation of force during activation is underestimated in experiments using bilayers.

During spreading, TCRs near synapse edges seemed to be pushed outward by polymerizing actin. This might have reflected associations between TCRs and barbed-end–associated factors that initiate actin polymerization. Alternatively, such patches might have represented nonligated, or even subplasmalemmal, collections of TCRs that moved anomalously. Ultimately, outward-moving microclusters centralized like interior microclusters, which suggested they were, or developed into, signaling microclusters. Inward flow from the periphery was biphasic; the initial, rapid centralization was associated with collapse of the dense lamellipodial actin meshwork, whereas slower centralization followed as microclusters moved into the interior. The slower centralization was probably associated with retrograde flow of actin[6,8]. As retrograde flow is dependent on continued actin depolymerization[36], localized depolymerization in the interior 'sink' would provide a mechanism for guiding TCRs to recycling regions. Organizing these flows probably requires the spatially regulated activity of cofilin, coronin and other related actin-depolymerizing proteins[37]. A published study showing blockade of TCR capping through the use of cofilin mimetic peptides supports that hypothesis[38]. We propose that depolymerization generates a low-viscosity 'sink' for inward microcluster flow. In this model, the 'motive' force is still polymerization[6,8]. However, a depolymerization-dependent mechanism in which flow is regulated by lower regional viscosity has appeal; this would explain how TCRs move inward discontinuously[7] at maximum rates that approach those of the retrograde flow of actin, whereas actin flows continuously[8]. The incorporation of microclusters into cSMACs, then, would be due to the 'squeezing' of microclusters and cSMACs into the same actin-poor region. Developing cSMACs also coupled to synapse movement. However, there was hysteresis in the cSMAC movement, which suggested passive coupling.

It has been reported that myosin II is deactivated in response to TCR triggering and that inhibition does not prevent TCR centralization or conjugate formation[23]. A subsequent study has reported instead that myosin II motor is required for the movement of TCRs into cSMACs, maintenance of adhesion to APCs and continued signaling[24]. Other published studies using blebbistatin have suggested that myosin II–mediated tension contributes to microcluster flow only in a brief, early phase of TCR centralization[25]. Finally, a published study of the use of blebbistatin to treat Jurkat human T lymphocyte cells has reported that the contraction of actinomyosin II arcs, in concert with actin depolymerization, directs TCR transport[25]. The disparities among these studies might reflect distinct motor requirements of mouse T cells, human T cells and Jurkat cells, differences in depletion efficiency, or comparison of cells selected for uptake of small interfering RNA to unselected cells in the control group. An issue has also arisen in some experiments as a result of the activation of protein crosslinking by blebbistatin with short-wavelength illumination[28,29]. The viability of T cells depleted of myosin II falls precipitously as the abundance of myosin II drops below the abundance that we have reported, which suggests that cells depleted in this way might be fundamentally compromised. Although tensioning by myosin II might enhance centralization under some conditions, our data have shown that it is dispensable.

It remains to be determined whether motile synapses are fundamentally different from the present models of immunological synapses. Our observations did not suggest a mechanistic distinction between stationary and motile synapses. A flexible framework for synapse formation, as presented here, can describe both the unstable synapses seen *in vivo* and highly organized sedentary synapses. This model does not require a coordinated relationship between the cSMAC and microcluster flow. Instead, the F-actin-poor 'sink' organizes TCR flow. This explains how synapses can organize signaling without motility arrest or the aggregation of TCRs into a cSMAC[16].

METHODS

Methods and any associated references are available in the online version of the paper.

Note: Supplementary information is available in the online version of the paper.

ACKNOWLEDGMENTS

We thank S. Rogers (University of Manchester) for the polynomial fit Gaussian weight function; R. Wedlich-Soldner (Max Planck Institute of Biochemistry) for Lifeact-GFP; B. Lillemeier (Salk Institute) and M. Davis (Stanford University) for the histidine-tagged ICAM construct; M. Werner and K. Austgen for assistance in preparing histidine-tagged ICAM; and J. Altman (US National Institutes of

Health Tetramer Facility at Emory University) for biotinylated pMHC monomers. Supported by the Cancer Research Institute (P.B.) and the US National Institutes of Health (AI52116 to M.F.K.).

AUTHOR CONTRIBUTIONS

P.B. and M.F.K. designed the experiments for **Figures 1–3** and **5–7** and P.B. did these experiments; P.B., J.J. and M.F.K. designed the experiments for **Figure 4** and P.B. and J.J. did these experiments; P.B. wrote the manuscript; J.J. contributed to editing of the manuscript; and M.F.K. edited and revised the manuscript.

COMPETING FINANCIAL INTERESTS

The authors declare no competing financial interests.

Published online at http://www.nature.com/doifinder/10.1038/ni.2364.
Reprints and permissions information is available online at http://www.nature.com/reprints/index.html.

1. Krummel, M.F., Sjaastad, M.D., Wülfing, C. & Davis, M.M. Differential clustering of CD4 and CD3ζ during T cell recognition. *Science* **289**, 1349–1352 (2000).
2. Grakoui, A. *et al.* The immunological synapse: a molecular machine controlling T cell activation. *Science* **285**, 221–227 (1999).
3. Wülfing, C. & Davis, M.M.A. Receptor/cytoskeletal movement triggered by costimulation during T cell activation. *Science* **282**, 2266–2269 (1998).
4. Monks, C.R.F., Freiberg, B.A., Kupfer, H., Sciaky, N. & Kupfer, A. Three-dimensional segregation of supramolecular activation clusters in T cells. *Nature* **395**, 82–86 (1998).
5. Yokosuka, T. *et al.* Newly generated T cell receptor microclusters initiate and sustain T cell activation by recruitment of Zap70 and SLP-76. *Nat. Immunol.* **6**, 1253–1262 (2005).
6. Varma, R., Campi, G., Yokosuka, T., Saito, T. & Dustin, M.L. T cell receptor-proximal signals are sustained in peripheral microclusters and terminated in the central supramolecular activation cluster. *Immunity* **25**, 117–127 (2006).
7. Mossman, K.D., Campi, G., Groves, J.T. & Dustin, M.L. Altered TCR signaling from geometrically repatterned immunological synapses. *Science* **310**, 1191–1193 (2005).
8. Kaizuka, Y., Douglass, A.D., Varma, R., Dustin, M.L. & Vale, R.D. Mechanisms for segregating T cell receptor and adhesion molecules during immunological synapse formation in Jurkat T cells. *Proc. Natl. Acad. Sci. USA* **104**, 20296–20301 (2007).
9. Dustin, M.L. & Springer, T.A. T-cell receptor cross-linking transiently stimulates adhesiveness through LFA-1. *Nature* **341**, 619–624 (1989).
10. Miller, M.J., Safrina, O., Parker, I. & Cahalan, M.D. Imaging the single cell dynamics of $CD4^+$ T cell activation by dendritic cells in lymph nodes. *J. Exp. Med.* **200**, 847–856 (2004).
11. Mempel, T.R., Henrickson, S.E. & von Andrian, U.H. T-cell priming by dendritic cells in lymph nodes occurs in three distinct phases. *Nature* **427**, 154–159 (2004).
12. Celli, S., Garcia, Z. & Bousso, P. CD4 T cells integrate signals delivered during successive DC encounters in vivo. *J. Exp. Med.* **202**, 1271–1278 (2005).
13. Gunzer, M. *et al.* Antigen presentation in extracellular matrix: interactions of T cells with dendritic cells are dynamic, shortlived, and sequential. *Immunity* **13**, 323–332 (2000).
14. Campi, G., Varma, R. & Dustin, M.L. Actin and agonist MHC-peptide complex-dependent T cell receptor microclusters as scaffolds for signaling. *J. Exp. Med.* **202**, 1031–1036 (2005).
15. Lee, K.-H. *et al.* The immunological synapse balances T cell receptor signaling and degradation. *Science* **302**, 1218–1222 (2003).
16. Friedman, R.S., Beemiller, P., Sorensen, C.M., Jacobelli, J. & Krummel, M.F. Real-time analysis of T cell receptors in naive cells in vitro and in vivo reveals flexibility in synapse and signaling dynamics. *J. Exp. Med.* **207**, 2733–2749 (2010).
17. Skokos, D. *et al.* Peptide-MHC potency governs dynamic interactions between T cells and dendritic cells in lymph nodes. *Nat. Immunol.* **8**, 835–844 (2007).
18. Negulescu, P.A., Krasieva, T.B., Khan, A., Kerschbaum, H.H. & Cahalan, M.D. Polarity of T cell shape, motility, and sensitivity to antigen. *Immunity* **4**, 421–430 (1996).
19. Sims, T.N. *et al.* Opposing effects of PKCθ and WASp on symmetry breaking and relocation of the immunological synapse. *Cell* **129**, 773–785 (2007).
20. Weiss, A., Imboden, J., Shoback, D. & Stobo, J. Role of T3 surface molecules in human T-cell activation: T3-dependent activation results in an increase in cytoplasmic free calcium. *Proc. Natl. Acad. Sci. USA* **81**, 4169–4173 (1984).
21. Ehrlich, J.S., Hansen, M.D.H. & Nelson, W.J. Spatio-temporal regulation of Rac1 localization and lamellipodia dynamics during epithelial cell-cell adhesion. *Dev. Cell* **3**, 259–270 (2002).
22. Beemiller, P., Jacobelli, J. & Krummel, M.F. Imaging and analysis of OT1 T cell activation on lipid bilayers. *Nat. Protoc.* published online, doi:10.1038/protex.2012.028 (1 July 2012).
23. Jacobelli, J., Chmura, S.A., Buxton, D.B., Davis, M.M. & Krummel, M.F. A single class II myosin modulates T cell motility and stopping, but not synapse formation. *Nat. Immunol.* **5**, 531–538 (2004).
24. Ilani, T., Vasiliver-Shamis, G., Vardhana, S., Bretscher, A. & Dustin, M.L. T cell antigen receptor signaling and immunological synapse stability require myosin IIA. *Nat. Immunol.* **10**, 531–539 (2009).
25. Yu, Y., Fay, N.C., Smoligovets, A.A., Wu, H.-J. & Groves, J.T. Myosin IIA modulates T cell receptor transport and CasL phosphorylation during early immunological synapse formation. *PLoS ONE* **7**, e30704 (2012).
26. Yi, J., Wu, X.S., Crites, T. & Hammer, J.A. Actin retrograde flow and acto-myosin II arc contraction drive receptor cluster dynamics at the immunological synapse in Jurkat T-cells. *Mol. Biol. Cell* **23**, 834–852 (2012).
27. Straight, A.F. *et al.* Dissecting temporal and spatial control of cytokinesis with a myosin II inhibitor. *Science* **299**, 1743–1747 (2003).
28. Kolega, J. Phototoxicity and photoinactivation of blebbistatin in UV and visible light. *Biochem. Biophys. Res. Commun.* **320**, 1020–1025 (2004).
29. Sakamoto, T., Limouze, J., Combs, C.A., Straight, A.F. & Sellers, J.R. Blebbistatin, a myosin II inhibitor, is photoinactivated by blue light. *Biochemistry* **44**, 584–588 (2005).
30. Jacobelli, J., Bennett, F.C., Pandurangi, P., Tooley, A.J. & Krummel, M.F. Myosin-IIA and ICAM-1 regulate the interchange between two distinct modes of T cell migration. *J. Immunol.* **182**, 2041–2050 (2009).
31. Jacobelli, J. *et al.* Confinement-optimized three-dimensional T cell amoeboid motility is modulated via myosin IIA–regulated adhesions. *Nat. Immunol.* **11**, 953–961 (2010).
32. Riedl, J. *et al.* Lifeact: a versatile marker to visualize F-actin. *Nat. Methods* **5**, 605–607 (2008).
33. Bubb, M., Senderowicz, A., Sausville, E., Duncan, K. & Korn, E. Jasplakinolide, a cytotoxic natural product, induces actin polymerization and competitively inhibits the binding of phalloidin to F-actin. *J. Biol. Chem.* **269**, 14869–14871 (1994).
34. Bubb, M., Spector, I., Beyer, B.B. & Fosen, K.M. Effects of Jasplakinolide on the Kinetics of Actin Polymerization. An explanation for certain *in vivo* observations. *J. Biol. Chem.* **275**, 5163–5170 (2000).
35. Bunnell, S.C., Kapoor, V., Trible, R.P., Zhang, W. & Samelson, L.E. Dynamic actin polymerization drives T cell receptor–Induced spreading: a role for the signal transduction adaptor LAT. *Immunity* **14**, 315–329 (2001).
36. Vallotton, P., Gupton, S.L., Waterman-Storer, C.M. & Danuser, G. Simultaneous mapping of filamentous actin flow and turnover in migrating cells by quantitative fluorescent speckle microscopy. *Proc. Natl. Acad. Sci. USA* **101**, 9660–9665 (2004).
37. Delorme, V. *et al.* Cofilin activity downstream of Pak1 regulates cell protrusion efficiency by organizing lamellipodium and lamella actin networks. *Dev. Cell* **13**, 646–662 (2007).
38. Eibert, S.M. *et al.* Cofilin peptide homologs interfere with immunological synapse formation and T cell activation. *Proc. Natl. Acad. Sci. USA* **101**, 1957–1962 (2004).

ONLINE METHODS

Mice. OT-I mice (which have transgenic expression of a TCR that recognizes the SIINFEKL peptide of ovalbumin bound to H-2K^b)[39] from Taconic were bred in-house. Mice with *lox*P-flanked alleles encoding myosin IIA (*Myh9*$^{fl/fl}$) have been described[31]; these were crossed with OT-I mice. Mice were housed and bred at the University of California, San Francisco, according to Laboratory Animal Resource Center guidelines. Protocols were approved by the Institutional Animal Care and Use Committee of the University of California.

Cells. CD8$^+$ OT-I T cell blasts were prepared from the lymph nodes of OT-I mice. Cells were retrovirally transduced with supernatants of CD3ζ-GFP- or Lifeact-GFP-expressing [Phoenix cells as described[40]. OT-I T cell blasts with conditional deficiency in myosin II were generated by transduction of proliferating *Myh9*$^{fl/fl}$ OT-I T cells with supernatants of Phoenix cells transfected with retrovirus expressing Cre-GFP[31]. T cell blasts were used 4–6 d after stimulation. On the day of imaging, live T cells were collected, stained as required for experiments, washed and then held on ice in complete RPMI medium without phenol red indicator until used for imaging. For labeling of surface TCRs, 2×10^6 cells were stained for 30 min on ice with 1 μg Alexa Fluor 568–labeled H57-597 antibody to TCRβ (Bio-X-Cell) in 0.1 ml complete RPMI medium without indicator.

For inhibition of actin depolymerization, stained, washed cells on ice were treated with 25–100 μM jasplakinolide. After 15 min, cells were transferred to a prewarmed bilayer well containing jasplakinolide at the same concentration used to treat the cells. For inhibition of actin polymerization, cells were incubated for 30 min at 37 °C with 10 μM cytochalasin D. For inhibition of myosin II activity, 50 μM (–)-blebbistatin (loaded as a racemic mixture of (+) enantiomers (inactive) and (–) enantiomers (active) at a concentration of 100 μM) was added to cells for 30 min at 22 °C before the addition of cells to a well preloaded with blebbistatin. DMSO (dimethyl sulfoxide) served as a control for drug treatments.

Reagents. Antibody H57-597 (anti-TCRβ) was from Bio-X-Cell and was conjugated to Alexa Fluor 568 at the hybridoma facility of the University of California, San Francisco. The dodecahistidine-tagged extracellular domain of ICAM1 (his-ICAM) was purified from the supernatant of High Five cells transfected with a baculovirus expression system, purified with nickel-affinity resin, followed by MonoQ, then Superdex FPLC, and then labeled with Alexa Fluor 488 through the use of Alexa Fluor 488 succinimidyl ester. Biotinylated H-2K^b loaded with SIINFEKL (from Beckman Coulter or the US National Institutes of Health Tetramer Facility) was used in monomeric form.

Lipid bilayers. Phospholipid mixtures consisting of 96.5% POPC (1-palmitoyl-2-oleoyl-sn-glycero-3-phosphocholine), 2% DGS (1,2-dioleoyl-sn-glycero-3-[(N-(5-amino-1-carboxypentyl)iminodiacetic acid)succinyl])–nickel–nitrilotriacetic acid, 1% biotinyl-Cap–PE (1,2-dioleoyl-sn-glycero-3-phosphoethanolamine-N-(cap biotinyl) (sodium salt) and 0.5% polyethylene glycol 5,000–PE (1,2-dioleoyl-sn-glycero-3-phosphoethanolamine-N-[methoxy(polyethylene glycol)-5000]) were mixed in a round-bottomed flask and dried. The next day, liposomes were prepared from the rehydrated lipid cakes by extrusion through filters (pore size, 100 nm) with a LiposoFast extruder (Avestin).

For the setup of lipid bilayers, dilutions of liposomes were applied to a rigorously cleaned LabTek II chambered coverglass (Nalge Nunc). Excess liposomes were rinsed away, and bilayers were then blocked in 1% BSA in PBS. Streptavidin was loaded in 1% BSA in PBS and then the excess streptavidin was washed away. Biotinylated pMHC and his-ICAM and were added to bilayers at loading concentrations of 2.5×10^2 to 2.5×10^7 fg/ml (biotinylated pMHC) and 62.5–500 ng/ml (his-ICAM). After proteins were loaded, bilayers were rinsed, inhibitors were added if needed, and bilayers were prewarmed before application of cells.

For the generation of standardized bilayers, the concentration of his-ICAM and biotinylated pMHC on bilayers was measured relative to that of cultured BMDCs pulsed with 100 ng/ml SIINFEKL peptide. Lipid bilayers were set up on silica microspheres (Bangs Labs) by the same procedure used for coverslip-supported bilayers. Microsphere bilayer standards and BMDCs were stained with anti-ICAM (YN1/1.7.4; Hybridoma Facility of the University of California, San Francisco) and antibody to SIINFEKL–H-2K^b (25-D1.16; eBiosciences) and were analyzed by flow cytometry. Except where indicated otherwise, 'stimulating bilayer' refers to a bilayer loaded with his-ICAM and pMHC under conditions that generate protein presentation similar to those generated by peptide-pulsed BMDCs.

Microscopy. A Zeiss Axiovert 200-M equipped with Laser TIRF slider was used for all imaging (Zeiss). For TIRF microscopy, a 100× Plan-Fluar with a numerical aperture of 1.45 or a 100× PlanApo objective lens with a numerical aperture of 1.45 was used. A DG-4 (Sutter Instruments) was used to provide epifluorescent illumination for Fura-2 ratiometric imaging and CellTracker Orange imaging. A40× PlanFluar objective with a numerical aperture of 1.3 was used for imaging of cell movements in widefield. For two-color TIRF imaging, a DV2, two-channel simultaneous imaging system (Photometrics) with a 560-nm longpass dichroic filter and 525-nm/50-nm and 605-nm/70-nm bandpass emission filters was used to split the camera field into two image channels for simultaneous imaging of GFP and Alexa Fluor 568. Images were collected by one of two cameras: an Evolve emCCD (Photometrics) or a Stanford Photonics XR-10MegaZ iCCD (Stanford Photonics). For TIRF image sequences acquired with the iCCD, QED InVivo (Media Cybernetics) software was used. For TIRF, FRAP and Fura ratiometric images acquired with the emCCD, Metamorph software was used (Universal Imaging).

For imaging of OT-I T cells interacting with the bilayers, 1×10^5 cells in 0.1 ml complete RPMI medium without phenol red indicator were added to the PBS (0.5 ml) overlaying the bilayer. For Fura ratiometric image time-lapse sequences, acquisition began as soon as the first cells tethered to the bilayer (typically within 1 min of the addition of cells). Fura-2 component images, consisting of 340 nm/10 nm or 380 nm/10 nm excitation with emission recorded at 520 nm/20 nm, were collected for 20 min at intervals of 15 s with exposures of 33–66 milliseconds. For TIRF time-lapse images, cells undergoing initial spreading onto bilayers were located, and TIRF images acquired for 3–5 min at intervals of 1 or 2 s with exposure lengths of 33–100 milliseconds. Cells were imaged until all cells had bound to the bilayers (typically 10–15 min) or, for imaging of jasplakinolide- or blebbistatin-treated cells, for 5 min after delivery of cells into wells.

Image analysis. MATLAB (The Mathworks) was used for all image arithmetic operations, such as filtering, background subtraction, masking and division. TCR microclusters were identified by polynomial fitting with the Gaussian weight method[41]. The microclusters identified were assigned to tracks with Imaris software (Andor) by transfer of the microcluster data with the ImarisXT MATLAB interface. Further track analysis, such as the categorization of tracks by their time of formation or calculation of movement vectors, was done after transfer of the assembled tracks to data structures in MATLAB. Cells were tracked through the use of Imaris software, with Fura-2 ratiometric images calculated and masked in MATLAB. Conversion of Fura-2 ratiometric intensities to calcium concentrations was done as described[42]. Detailed descriptions of the image processing is available[22].

Prism (GraphPad Software) was used for statistical analyses. The Mann-Whitney *U*-test or Student's *t*-test, where appropriate, were used for comparison of samples. For comparison of multiple groups, a one-way analysis of variance ($\alpha = 0.05$) was used with Dunnett's post-test.

39. Hogquist, K.A. *et al.* T cell receptor antagonist peptides induce positive selection. *Cell* **76**, 17–27 (1994).
40. Friedman, R.S., Jacobelli, J. & Krummel, M.F. Surface-bound chemokines capture and prime T cells for synapse formation. *Nat. Immunol.* **7**, 1101–1108 (2006).
41. Rogers, S.S., Waigh, T.A., Zhao, X. & Lu, J.R. Precise particle tracking against a complicated background: polynomial fitting with Gaussian weight. *Phys. Biol.* **4**, 220–227 (2007).
42. Grynkiewicz, G., Poenie, M. & Tsien, R. A new generation of Ca^{2+} indicators with greatly improved fluorescence properties. *J. Biol. Chem.* **260**, 3440–3450 (1985).

doi:10.1038/ni.2364